mathematics

MDPI

Article

Energy Transfer through a Magnetized Williamson Hybrid Nanofluid Flowing around a Spherical Surface: Numerical Simulation

Oruba Ahmad Saleh Alzu'bi [1], Firas A. Alwawi [2,*], Mohammed Z. Swalmeh [3,4], Ibrahim Mohammed Sulaiman [5,6], Abdulkareem Saleh Hamarsheh [2] and Mohd Asrul Hery Ibrahim [4]

1 Department of Mathematics, Faculty of Science, Al Balqa'a Applied University, Salt 19117, Jordan
2 Department of Mathematics, College of Sciences and Humanities in Al-Kharj, Prince Sattam bin Abdulaziz University, Al-Kharj 11942, Saudi Arabia
3 Department of Service Courses, Faculty of Arts and Sciences, Aqaba University of Technology, Aqaba 77110, Jordan
4 Faculty of Entrepreneurship and Business, Universiti Malaysia Kelantan, Kota Bharu 16100, Kelantan, Malaysia
5 School of Quantitative Sciences, Universiti Utara Malaysia, Sintok 06010, Kedah, Malaysia
6 Institute of Strategic Industrial Decision Modelling (ISIDM), Universiti Utara Malaysia, Sintok 06010, Kedah, Malaysia
* Correspondence: f.alwawi@psau.edu.sa

Abstract: A computational simulation of Williamson fluid flowing around a spherical shape in the case of natural convection is carried out. The Lorentz force and constant wall temperature are taken into consideration. In addition, upgrader heat transfer catalysts consisting of multi-walled carbon tubes, molybdenum disulfide, graphene oxide, and molybdenum disulfide are employed. The Keller box approach is used to solve the mathematical model governing the flow of hybrid Williamson fluid. To validate our findings, the key parameters in the constructed model are set to zero. Next, the extent of the agreement between our results and published results is observed. Numerical and graphical results that simulate the impressions of key parameters on physical quantities related to energy transmission are obtained, discussed, and analyzed. According to the results of this study, increasing the value of the Weissenberg number causes an increase in both the fluid temperature and drag force, while it also leads to a decrease in both the velocity of the fluid and the rate of energy transmission. Increasing the magnetic field intensity leads to a reduction in the rate of heat transfer, drag force, and fluid velocity while it has an appositive effect on temperature profiles.

Keywords: free convection; hybrid Williamson nanofluid; magnetized host fluid; spherical surface; Tiwari–Das model

MSC: 76B99

Citation: Alzu'bi, O.A.S.; Alwawi, F.A.; Swalmeh, M.Z.; Sulaiman, I.M.; Hamarsheh, A.S.; Ibrahim, M.A.H. Energy Transfer through a Magnetized Williamson Hybrid Nanofluid Flowing around a Spherical Surface: Numerical Simulation. *Mathematics* **2022**, *10*, 3823. https://doi.org/10.3390/math10203823

Academic Editors: Katta Ramesh and Rama Subba Reddy Gorla

Received: 13 September 2022
Accepted: 12 October 2022
Published: 16 October 2022

1. Introduction

Recently, researchers in the field of hydrodynamics have focused their studies on non-Newtonian fluids because of the latter's important engineering applications. The result of this focus is the emergence of many mathematical models that attempt to simulate the behavior of these fluids. One of the most important non-Newtonian fluid models considered in several papers is the Williamson fluid model proposed by Williamson [1]. He presented a governing equation explaining pseudoplastic fluid flow, thereby addressing the problems of mass transfer of the pseudoplastic, in which the shear-thinning features of non-Newtonian fluids were highlighted, and laboratory experiments were presented to examine the proposed approach. Later on, several studies extended the Williamson model in different directions. Lyubimov and Perminov [2] investigated the tinny film movement

of a Williamson fluid via an inclined surface in the gravitational field. The authors analyzed the effect of the tangential and latter vibrations of the solid surface on layer flow and presented the results of the experiments, showing that a pronounceable average fluid flow was generated by the vibrations despite the weak gravitational field where the film is at rest. Nadeem and Akram [3] presented a study on the peristaltic transit of Williamson liquid in an asymmetric channel. Their study concluded that the curves of the pressure increase for large values of the Williamson factor are not linear, but for small values of the Williamson factor, they tend to behave as Newtonian liquids. Under the effects of nanoparticles, Nadeem and Hussain [4] investigated Williamson fluids' two-dimensional flow over a stretching sheet. Nanomaterial chemically reactive flow-outcomes were modelled and analyzed using the rheological expressions of Williamson fluid by Hayat et al. [5]. The work considered a nonlinear bidirectional stretching sheet for the simulation. The outcome of the study shows that for higher values of magnetic parameters, the velocity always decays in the direction of travel. The Williamson fluid assessment of time-dependent flow was studied by Subbarayudu et al. [6]. The authors considered the radiative blood flow of the Williamson fluid against a wedge. Waqas et al. [7] and Hayat et al. [8] looked at incompressible, steady 2D nonlinear forced or mixed convective Williamson fluid flow on stretchable or flat surfaces, as well as the heat generation interaction of Williamson fluid flow in nonlinear forced or mixed convection subjects.

In 1995, Choi and Eastman [9] incorporated nanotechnology into the field of energy transmission for the first time, and this led to a quantum leap in improving the ability of the base fluids to transfer energy. Eastman et al. [10] affirmed that copper ultrafine particles can boost the heat transport properties of ethylene glycol. Chon et al. [11] reported the effect of temperature and nanoparticle size on the nanofluid's thermal characteristics. Xuan and Li [12] identified the most critical factors influencing the rate of heat transfer, which may also be influenced by the factors addressed by the authors of [13–15]. Recently, Tiwari and Das [16] constructed a mathematical model that included highlighting the effect of the ultrafine particle-volume fraction on the physical properties relevant to heat transfer. Subsequently, many of the mathematical models that govern the issues associated with laminar boundary layers were extensions of the Tiwari and Das model. Tham et al. [17,18] utilized the Tiwari and Das model to report the combined convection flow past a sphere and cylinder. Dinarvand et al. [19] applied the Tiwari and Das model to simulate the magneto-combined convection of nanofluid about a vertical permeable cylinder. Swalmeh et al. [20–22] examined the natural convection flow of micropolar nanoliquid around spherical and cylindrical surfaces. Alwawi et al. [23–27] reported the effect of the magnetic field on the heat transmission rate of Casson nanofluid employing the Tiwari–Das model. See also [28–32].

The second leap related to heat transfer has come from upgrading the ultrafine particles by synthesizing more than one compound to create a hybrid nanomaterial with optimized thermal features. Turcu et al. [33] are recognized as being among the first to synthesize hybrid nanomaterials from polypyrrole-CNTs and Fe_3O_4–MWCNTs. Suresh et al. [34] produced a hybrid material with improved thermal conductivity, composed of copper and aluminum oxides. Baghbanzadeh et al. [35] described a technique for combining SiO_2 with MWCNTs to create hybrid ultrafine particles, as well as showing the best SiO_2 to MWCNTs ratio to generate the maximum thermal conductivity for the hybrid synthesis material. Zhou et al. [36] fabricated a polymer hybrid nanomaterial with excellent thermal conductivity. Leong et al. [37] presented an interesting review of hybrid nanocomposites, their synthesis methods, and the most important aspects to be taken into consideration, such as thermal conductivity, stability of the host fluid, and others. More comprehensive studies are provided by the authors of [38–41]. Accordingly, several numerical investigations have been carried out in an attempt to predict the behavior of hybrid nanofluids. Devi and Devi [42] confirmed in their numerical study of the hybrid nanoliquid flowing around a permeable sheet that hybrid nanoparticles of Al_2O_3-Cu can give water a higher rate of energy transmission than Cu mono nanoparticles. Hayat and Nadeem [43] highlighted 3D-hybrid

nanofluid flow over a stretching surface, taking into consideration radiation effects, heat creation, and chemical reaction. Subhani and Nadeem [44] carried out a computational analysis comparing the heat transfer rates of a mono and hybrid micropolar nanofluid flowing in a porous medium on a stretching surface. Khashi'ie et al. [45] simulated the magneto-mixed convection flow of hybrid nonliquid around a shrinking cylinder with the assistance of the Tiwari–Das model. Alwawi et al. [46] discussed heat transfer boosters generated by a transient magnetic field through a hybrid fluid moving around a cylinder. It is worth mentioning here that these comprehensive studies [47–50] used the second grade of the ultrafine particles and combined the models of Tiwari–Das and Williamson to simulate the behavior of these fluids; which behavior is the closest to this study and one of the reasons that motivated us to proceed with this investigation. As a result of these massive experimental and numerical studies, we observed the wide-range inclusion of hybrid particles to enhance heat transfer in conceivable primary applications such as electronic and manufacturing cooling, solar energy, heat exchangers, etc. [51–53]. In the case of laminar-boundary layer flow, there are numerous effective approximation methods for dealing with the problems of heat transfer through fluids [54–58]. The Keller Box approximation was used in this paper because it is one of the best approximations for dealing with laminar-boundary layer problems, has many distinguishing characteristics, and has been widely used for more than three decades.

Based on the above literature, the fabricated molybdenum disulfide nanosolid (MoS_2) on the one hand, and multi-walled carbon nanotubes (MWCNTs) and graphene oxide (GO) on the other hand, are used to support the thermal feature of the host Williamson fluid, which flows over a spherical surface. An applied magnetic field is also included because of its substantial impact on the energy transmission characteristics of hybrid nanofluids and its unlimited use in many engineering and industrial applications. In addition, the state of convection produced by natural means is considered. To the best of our knowledge, there is no study available that investigates this problem. Accordingly, in this report, the relevant equations are solved by converting PDEs into the dimensionless form using an appropriate conversion. The implicit Keller box finite difference method is used for the local similar solution of dimensionless governing equations and the flow and energy transport characteristics of the Williamson hybrid nanofluid past a sphere. Computational outcomes are computed, addressed, and analyzed in the form of tables and figures in order to simulate the effects of key parameters on the Nusselt number, velocity, skin friction coefficient, and temperature.

2. Problem Description

A convection produced by natural means in an electro-conductive Williamson hybrid nanofluid flowing over a spherical body under the influence of a magnetic field B_0 was assumed, as shown in Figure 1. The constant wall temperature $T_w > T_\infty$ as well as an applied magnetic field are considered. T_w stands for the wall temperature, T_∞ is the ambient temperature. Additionally, $\overline{\eta}$ is the curvilinear coordinate over the sphere border, measuring its surface's circumference, and $\overline{\gamma}$ is the distance normal to the sphere's surface.

According to the preceding considerations, governing equations could be formed as follows (see [23,59,60]):

$$\frac{\partial r\overline{u}}{\partial \overline{\eta}} + \frac{\partial r\overline{v}}{\partial \overline{\gamma}} = 0, \tag{1}$$

$$\rho_{Hnf}\left(\hat{u}\frac{\partial \overline{u}}{\partial \overline{\eta}} + \hat{v}\frac{\partial \overline{u}}{\partial \overline{\gamma}}\right) = -\frac{\partial \overline{P}}{\partial \overline{\eta}} + \sqrt{2}v\Gamma\left(\frac{\partial^2 \overline{u}}{\partial \overline{\gamma}^2}\frac{\partial \overline{u}}{\partial \overline{\gamma}}\right) + \mu_{Hnf}\left(\frac{\partial^2 \overline{u}}{\partial \overline{\gamma}^2} + \frac{\partial^2 \overline{u}}{\partial \overline{\eta}^2}\right) + \rho_{Hnf}\beta_{Hnf}g(T - T_\infty)\sin\left(\frac{\overline{\eta}}{a}\right) - \sigma_{Hnf}B_0^2\hat{u}, \tag{2}$$

$$\rho_{Hnf}\left(\overline{u}\frac{\partial \overline{u}}{\partial \overline{\eta}} + \overline{v}\frac{\partial \overline{u}}{\partial \overline{\gamma}}\right) = -\frac{\partial \overline{P}}{\partial \overline{\gamma}} + \sqrt{2}v\Gamma\left(\frac{\partial^2 \overline{u}}{\partial \overline{\gamma}^2}\frac{\partial \overline{u}}{\partial \overline{\gamma}}\right) + \mu_{Hnf}\left(\frac{\partial^2 \overline{u}}{\partial \overline{\gamma}^2} + \frac{\partial^2 \overline{u}}{\partial \overline{\eta}^2}\right) + \rho_{Hnf}\beta_{Hnf}g(T - T_\infty)\cos\left(\frac{\overline{\eta}}{a}\right) - \sigma_{Hnf}B_0^2\overline{u}, \tag{3}$$

$$\overline{u}\frac{\partial T}{\partial \overline{\eta}} + \overline{v}\frac{\partial T}{\partial \overline{\gamma}} = \alpha_{Hnf}\left(\frac{\partial^2 T}{\partial \overline{\gamma}^2} + \frac{\partial^2 T}{\partial \overline{\eta}^2}\right), \tag{4}$$

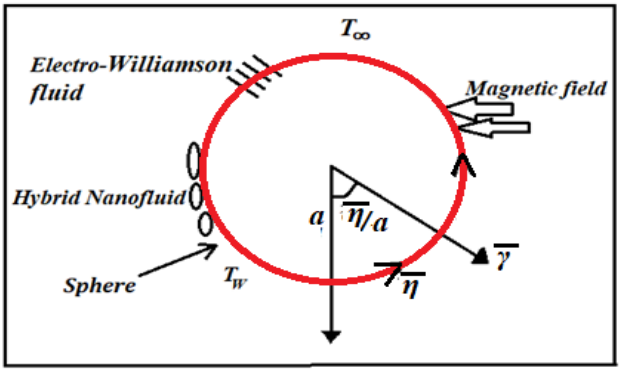

Figure 1. MHD Williamson hybrid nanofluid physical model.

The constant wall temperature boundary condition of the above governing equations will be defined as:

$$\begin{aligned} \overline{u} = \overline{v} = 0,\ T = T_w \ \ at \quad \overline{\gamma} = 0, \\ \overline{u} \to 0,\ T \to T_\infty,\ p \to p_\infty \ \ at \quad \overline{\gamma} \to \infty, \end{aligned} \tag{5}$$

where $\overline{u}$ and $\overline{v}$ are referents for the velocity components along $\overline{\eta}$, $\overline{\gamma}$ axes, respectively. $\overline{r}(\overline{\eta})$ is called the radial distance from the symmetrical axis to the surface of the sphere. P is pressure and Γ is fluid relaxation time.

To convert the dimensional governing equations to the non-dimensional, we utilize the following non-dimensional variables, as follows:

$$\begin{aligned} \omega = \left(\frac{\overline{\eta}}{a}\right)\gamma = \mathrm{Gr}^{1/4}\left(\frac{\overline{\gamma}}{a}\right),\ u = \left(\frac{a}{\nu_f}\right)\mathrm{Gr}^{-1/2}\overline{u}\,, v = \left(\frac{a}{\nu_f}\right)\mathrm{Gr}^{-1/4}\overline{v} \\ \theta = \frac{T - T_\infty}{T_w - T_\infty}, p = \frac{\hat{p} - p_\infty}{\rho_f(v_f^2/a^2)}, \end{aligned} \tag{6}$$

where Gr is determined physically as a non-dimensional number and symbolizes the ratio of the buoyancy forces to the viscous forces, and it can also be defined as $\mathrm{Gr} = g\beta_f(T_w - T_\infty)\frac{a^3}{\nu_f^2}$ (see [61]). Pr is non-dimensional quantity, and it is a particular physical feature of fluids only. It is examined by considering the proportion of the velocity against the thermal of boundary layer thickness. On the other hand, the Prandtl number law is equal to momentum diffusivity over thermal diffusivity ($\mathrm{Pr} = \frac{v_f}{\alpha_f}$) (see [62]).

Table 1 presents the thermo-physical characteristics of the hybrid nanofluids and mono nanofluids on which this study is based.

Table 1. Thermo-physical characteristics [49].

Properties of the Mono Nanofluid	Properties of the Hybrid Nanofluid
$\rho_{nf} = (1-\omega)\rho_f + \omega\rho_s$, $(\rho c_p)_{nf} = (1-\omega)(\rho c_p)_f + \omega(\rho c_p)_s$, $\beta_{nf} = (1-\omega)\beta_f + \omega\beta_s$ $\mu_{nf} = \frac{\mu_f}{(1-\omega)^{2.5}}$, $\frac{k_{nf}}{k_f} = \frac{(k_s+2k_f)-2\omega(k_f-k_s)}{(k_s+2k_f)+\omega(k_f-k_s)}$, $\alpha_{nf} = \frac{k_{nf}}{(\rho c_p)_{nf}}$, $\frac{\sigma_{nf}}{\sigma_f} = 1 + \frac{3(\sigma-1)\omega}{(\sigma+2)-(\sigma-1)\omega}$, $\sigma = \frac{\sigma_s}{\sigma_f}$	$\rho_{Hnf} = (1-\omega_2)[(1-\omega_1)\rho_f + \omega_1\rho_{s1}] + \omega_2\rho_{s2}$, $(\rho c_p)_{Hnf} = (1-\omega_2)[(1-\omega_1)(\rho Cp)_f + \omega_1(\rho Cp)_{s1}] + \omega_2(\rho Cp)_{s2}$, $\beta_{Hnf} = (1-\omega_2)[(1-\omega_1)\beta_f + \omega_1\beta_{s1}] + \omega_2\beta_{s2}$. $\mu_{hnf} = \frac{\mu_f}{(1-\omega_1)^{2.5}(1-\omega_2)^{2.5}}$, $\frac{k_{Hnf}}{k_{bf}} = \frac{k_{s2}+2k_{bf}-2\omega_2(k_{bf}-k_{s2})}{k_{s2}+2k_{bf}+\omega_2(k_{bf}-k_{s2})}$, $\frac{k_{bf}}{k_f} = \frac{k_{s1}+2k_f-2\omega_1(k_f-k_{s1})}{k_{s1}+2k_f+\omega_1(k_f-k_2)}$, $\alpha_{Hnf} = \frac{k_{Hnf}}{(\rho cp)_{Hnf}}$, $\frac{\sigma_{Hnf}}{\sigma_{bf}} = [\frac{\sigma_{s2}+2\sigma_{bf}-2\omega_2(\sigma_{bf}-\sigma_{s2})}{\sigma_{s2}+2\sigma_{bf}+\omega_2(\sigma_{bf}-\sigma_{s2})}]$, $\frac{\sigma_{bf}}{\sigma_f} = [\frac{\sigma_{s1}+2\sigma_f-2\omega_1(\sigma_f-\sigma_{s1})}{\sigma_{s1}+2\sigma_f+\omega_1(\sigma_f-\sigma_{s1})}]$

Here $\varpi, \rho, (\rho c_p), \beta$ are called nanoparticle volume fraction, density, heat capacity, and thermal expansion, respectively. In addition, μ, k, α, σ refer to dynamic viscosity, thermal conductivity, thermal diffusivity, and electrical conductivity, respectively. Furthermore, the subscripts s, f, nf, hnf symbolize solid, host fluid, nanoliquid, and hybrid nanoliquid, respectively.

Using Equation (6), the described hybrid nanofluid properties in Table 1, and the useful boundary layer approximations technique ($Gr \to \infty$), we obtain $(\partial p/\partial \eta) = 0$ and $(\partial p/\partial \gamma) = 0$. In other words, this provides the next equations, those containing Williamson hybrid nanofluid effects and the magnetic field at the momentum equation:

$$\frac{\partial ru}{\partial \eta} + \frac{\partial rv}{\partial \gamma} = 0 \tag{7}$$

$$\begin{aligned} u\frac{\partial u}{\partial \eta} + v\frac{\partial u}{\partial \gamma} &= \frac{\rho_f}{\rho_{Hnf}}\left(\frac{1}{(1-\varpi_1)^{2.5}(1-\varpi_2)^{2.5}}\right)\frac{\partial^2 u}{\partial \gamma^2} + \mathrm{We}\left(\frac{\partial^2 u}{\partial \gamma^2}\frac{\partial u}{\partial \gamma}\right) \\ &+ \frac{1}{\rho_{Hnf}}\left((1-\varpi_2)[(1-\varpi_1)\rho_f + \varpi_1\frac{\rho_{s1}\beta_{s1}}{\beta_f}] + \varpi_2\frac{\rho_{s2}\beta_{s2}}{\beta_f}\right)\theta\sin\eta - \frac{\rho_f}{\rho_{Hnf}}\frac{\sigma_{Hnf}}{\sigma_f}\mathrm{M}u, \end{aligned} \tag{8}$$

$$\begin{aligned} &u\frac{\partial \theta}{\partial \eta} + v\frac{\partial \theta}{\partial \gamma} \\ &= \frac{1}{\mathrm{Pr}}\left[\frac{k_{Hnf}/k_f}{(1-\varpi_2)[(1-\varpi_1)+\varpi_1(\rho Cp)_1/(\rho Cp)_f]+\varpi_2(\rho Cp)_{s2}/(\rho Cp)_f}\right]\frac{\partial^2 \theta}{\partial \gamma^2}, \end{aligned} \tag{9}$$

In the previous system of equations, We is a non-dimensional parameter measuring the Fluid relaxation time Γ, and it is described as $\mathrm{We} = \frac{\Gamma\eta\ Gr^{3/4}}{a^3}$. $\mathrm{M} = \left(\frac{\sigma_f B_0^2 a^2 \mathrm{Gr}^{-1/2}}{\rho_f v_f}\right)$ is the magnetic parameter. Substituting the properties in Table 1 and Equation (6) yields the following non-dimensional form of boundary condition:

$$\begin{aligned} u = v = 0,\ \ \theta = 1,\ \ \text{at}\ \ \gamma = 0, \\ u \to 0,\ \ \theta \to 0, p \to 0,\ \ \text{as}\ \ \gamma \to \infty. \end{aligned} \tag{10}$$

The following transformation variables are effective in solving Equations (7)–(10), which are described as: (see [47])

$$\psi = \eta f(\eta, \gamma), \quad \theta = \theta(\eta, \gamma), \tag{11}$$

this is consistent with the following formula:

$$u = \frac{\partial \psi}{\partial \gamma} \text{ and } v = -\frac{\partial \psi}{\partial \eta} \tag{12}$$

that satisfies the continuity equation, where ψ is the stream function.

Thus, the reduction in the governing partial differential equations by substituting the transformation variables (11) and (12) is completed as shown below:

$$\begin{aligned} &\frac{\rho_f}{\rho_{Hnf}}\left(\frac{1}{(1-\varpi_1)^{2.5}(1-\varpi_2)^{2.5}}\right)\frac{\partial^3 f}{\partial \gamma^3} + \mathrm{We}\frac{\partial^3 f}{\partial \gamma^3}\frac{\partial^2 f}{\partial \gamma^2} + (1+\eta\cot\eta)f\frac{\partial^2 f}{\partial \gamma^2} - \left(\frac{\partial f}{\partial \gamma}\right)^2 + \\ &\frac{1}{\rho_{Hnf}}\left((1-\varpi_2)[(1-\varpi_1)\rho_f + \varpi_1\frac{\rho_{s1}\beta_{s1}}{\beta_f}] + \varpi_2\frac{\rho_{s1}\beta_{s2}}{\beta_f}.\right)\frac{\sin\eta}{\eta}\ \theta - \frac{\rho_f}{\rho_{Hnf}}\frac{\sigma_{Hnf}}{\sigma_f}\mathrm{M}\ \frac{\partial f}{\partial \gamma} \\ &= \eta\left(\frac{\partial f}{\partial \gamma}\frac{\partial^2 f}{\partial^2} - \frac{\partial f}{\partial \eta}\frac{\partial^2 f}{\partial \gamma^2}\right) \end{aligned} \tag{13}$$

$$\begin{aligned} &\frac{1}{\mathrm{Pr}}\left[\frac{k_{Hnf}/k_f}{(1-\varpi_2)[(1-\varpi_1)+\varpi_1(\rho Cp)_1/(\rho Cp)_f]+\varpi_2(\rho Cp)_{s2}/(\rho Cp)_f}\right]\frac{\partial^2 \theta}{\partial \gamma^2} \\ &+(1+\eta\cot\eta)f\frac{\partial \theta}{\partial \gamma} = \eta\left(\frac{\partial f}{\partial \gamma}\frac{\partial \theta}{\partial \eta} - \frac{\partial f}{\partial \eta}\frac{\partial \theta}{\partial \gamma}\right), \end{aligned} \tag{14}$$

subject to:

$$\begin{array}{c} f = \frac{\partial f}{\partial \gamma} = 0, \theta = 1 \ \text{ at } \ \gamma = 0, \\ \frac{\partial f}{\partial \gamma} \to 0, \ \ \theta \to 0, \ \ \text{as } \ \gamma \to \infty. \end{array} \tag{15}$$

Assuming that ϖ is approximately equal to 0 (at the stagnation point), Equations (13)–(15) are modified as follows:

$$\begin{array}{c} \frac{\rho_f}{\rho_{Hnf}}\left(\frac{1}{(1-\omega_1)^{2.5}(1-\omega_2)^{2.5}}\right)\frac{\partial^3 f}{\partial \gamma^3} + \mathrm{We}\frac{\partial^3 f}{\partial \gamma^3}\frac{\partial^2 f}{\partial \gamma^2} + 2f\frac{\partial^2 f}{\partial \gamma^2} - \left(\frac{\partial f}{\partial \gamma}\right)^2 + \\ \frac{1}{\rho_{Hnf}}\Big((1-\omega_2)[(1-\omega_1)\rho_f + \omega_1\frac{\rho_{s1}\beta_{s1}}{\beta_f}] + \omega_2\frac{\rho_{s1}\beta_{s2}}{\beta_f}.\Big)\theta - \frac{\rho_f}{\rho_{Hnf}}\ \frac{\sigma_{Hnf}}{\sigma_f}\mathrm{M}\ \ \frac{\partial f}{\partial \gamma} = 0, \end{array} \tag{16}$$

$$\begin{array}{c} \frac{1}{\mathrm{Pr}}\left[\frac{k_{hnf}/k_f}{(1-\vartheta_2)[(1-\vartheta_1)+\vartheta_1(\rho Cp)_1/(\rho Cp)_f]+\vartheta_2(\rho Cp)_{s2}/(\rho Cp)_f}\right]\frac{\partial^2 \theta}{\partial \gamma^2} \\ +2f\frac{\partial \theta}{\partial \gamma} = 0 \end{array} \tag{17}$$

with the modified boundary conditions:

$$\begin{array}{c} f(0,\gamma) = f'(0,\gamma) = 0, \ \theta(0,\gamma) = 1 \ \text{ as } \ \gamma = 0, \\ f'(0,\gamma) \to 0, \ \ \theta(0,\gamma) \to 0 \ \text{ as } \ \gamma \to \infty, \end{array} \tag{18}$$

Our attention focuses on the skin friction C_f and Nusselt number Nu, which are closely related to energy transfer C_f and Nu given by Swalmeh [59] as:

$$C_f \ = \ \left(\frac{\tau_w}{\rho_f U_\infty^2}\right), \ Nu = \left(\frac{aq_w}{k_f(T_w - T_\infty)}\right), \tag{19}$$

where

$$\tau_w = \mu_{Hnf}\left(\frac{\partial \overline{u}}{\partial \overline{\gamma}} + \left[\frac{\Gamma}{\sqrt{2}}\left(\frac{\partial \overline{u}}{\partial \overline{\gamma}}\right)^2\right]\right)_{\overline{\gamma}=\,0}, q_w = -\,k_{Hnf}\left(\frac{\partial T}{\partial \overline{\gamma}}\right)_{\overline{\gamma}=\,0} \tag{20}$$

C_f and Nu are reformulated into the following forms, using Equations (6) and (10):

$$C_f = \mathrm{Gr}^{-1/4}\frac{1}{(1-\omega_1)^{2.5}(1-\omega_2)^{2.5}}\omega\left(\frac{\partial^2 f}{\partial \gamma^2}\ (\eta,0) + \frac{\mathrm{We}}{2}\left(\frac{\partial f}{\partial \gamma}(\eta,0)\right)^2\right), Nu = \ -\mathrm{Gr}^{1/4}\frac{k_{Hnf}}{k_f}\frac{\partial \theta}{\partial \gamma}\ (\omega,0), \tag{21}$$

All parameters and symbols are shown in the nomenclature list.

3. Numerical Techniques

In this section, an efficient numerical procedure called the Keller box method is used for obtaining numerical solutions to Equations (13)–(15). Firstly, the Keller box method involves a finite difference scheme that reduces the order of PDEs to the system of first-order equations. Now, we begin by introducing the independent functions:

$$u(\eta,\gamma) = f'(\eta,\gamma), \ v(\eta,\gamma) = f''(\eta,\gamma), s(\eta,\gamma) = \theta(\eta,\gamma), \tag{22}$$

$$f' = u, \tag{23}$$

$$u' = v = f'', \tag{24}$$

$$\theta' = t, \tag{25}$$

Using the above transformation, Equations (13)–(15) can be represented in the following form:

$$\begin{aligned}&\frac{\rho_f}{\rho_{Hnf}}\left(\frac{1}{(1-\omega_1)^{2.5}(1-\omega_2)^{2.5}}\right)v' + \mathrm{We}\, v'v + (1+\eta\cot\eta)fv - (u)^2 + \\ &\frac{1}{\rho_{Hnf}}\left((1-\omega_2)[(1-\omega_1)\rho_f + \omega_1\tfrac{\rho_{s1}\beta_{s1}}{\beta_f}] + \omega_2\tfrac{\rho_{s1}\beta_{s2}}{\beta_f}.\right)\frac{\sin\eta}{\eta}\, s - \frac{\rho_f}{\rho_{Hnf}}\,\frac{\sigma_{Hnf}}{\sigma_f}\mathrm{M}\ u \\ &= \eta\left(u\frac{\partial u}{\partial\eta} - \frac{\partial f}{\partial\eta}v\right),\end{aligned} \tag{26}$$

$$\begin{aligned}&\frac{1}{\mathrm{Pr}}\left[\frac{k_{Hnf}/k_f}{(1-\omega_2)[(1-\omega_1)+\omega_1(\rho Cp)_1/(\rho Cp)_f]+\omega_2(\rho Cp)_{s2}/(\rho Cp)_f}\right]\theta'' \\ &+(1+\eta\cot\eta)f\frac{\partial\theta}{\partial\gamma} = \eta\left(f'\frac{\partial\theta}{\partial\eta} - \frac{\partial f}{\partial\eta}\theta'\right),\end{aligned} \tag{27}$$

where the primes symbol indicates differentiation of the variable γ. In addition, the boundary conditions (16) are transformed into:

$$\begin{aligned}&f(\eta,0) = 0, f(\eta,0) = 0,\ \theta = 1, \\ &f'(\eta,\infty) = 0,\ \ \theta(\eta,\infty) = 0,\end{aligned} \tag{28}$$

To make the steps mesh points in a two-dimensional η-γ plane, define k^n and h_n of the related step distances in η and γ orientations, respectively, as shown in Figure 2.

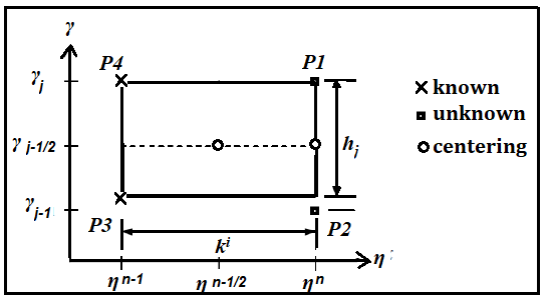

Figure 2. The rectangle of difference method.

The mesh points are indicated below:

$$\begin{aligned}&\gamma_0 = 0,\ \ \gamma_i = \gamma_{i-1} + h_i, i = 0,1,2,3,\ldots,J.\gamma_\infty = \gamma_J, \\ &\eta^0 = 0,\ \ \eta^i = \eta^i = \eta^{i-1} + k^i, i = 0,1,2,3,\ldots,N.\end{aligned} \tag{29}$$

For any independent quantities, midpoint and first derivative in the η-direction and γ-direction, placed by finite difference, is employed as follows:

$$\begin{aligned}()^{n-1/2}_{j-1/2} &= \frac{1}{4}\left(()^n_j + ()^n_{j-1} + ()^{n-1}_j + ()^{n-1}_{j-1}\right) \\ \left(\frac{\partial()}{\partial\gamma}\right)^{n-1/2}_{j-1/2} &= \frac{1}{2h_j}\left(()^n_j - ()^n_{j-1} + ()^{n-1}_j - ()^{n-1}_{j-1}\right) \\ \left(\frac{\partial()}{\partial\omega}\right)^{n-1/2}_{j-1/2} &= \frac{1}{2k^n}\left(()^n_j - ()^n_{j-1} + ()^{n-1}_j - ()^{n-1}_{j-1}\right)\end{aligned} \tag{30}$$

The following are finite difference approximations of Equations (23)–(25) and (26)–(27) about the midpoint $(\eta_n, \gamma_{j-1/2})$:

$$f^n_j - f^n_{j-1} = h_j\left(u^n_{j-1/2}\right), \tag{31}$$

$$u^n_j - u^n_{j-1} = h_j\left(v^n_{j-1/2}\right), \tag{32}$$

$$s_j^n - s_{j-1}^n = h_j\left(t_{j-1/2}^n\right), \tag{33}$$

$$\begin{aligned}
&\frac{\rho_f}{\rho_{Hnf}}\left(\frac{1}{(1-\omega_1)^{2.5}(1-\omega_2)^{2.5}}\right)\left(v_j - v_{j-1}\right) + \mathrm{We}\left(v_j + v_{j-1}\right)\left(v_j - v_{j-1}\right) + \\
&(1+\xi+\eta\cot\eta)\tfrac{\xi}{4}h_j(f_j+f_{j-1})(v_j+v_{j-1}) - \left(\tfrac{1+\xi}{4}\right)h_j\,(u_j+u_{j-1})^2 - \\
&\tfrac{1}{2}\tfrac{\rho_f\sigma_{nf}}{\rho_{nf}\sigma_f}\,\mathrm{M}h_j\;(u_j+u_{j-1}) + \left(\tfrac{1+\xi}{2}\right)h_j v_{j-1/2}^{n-1}(f_j+f_{j-1}) - \left(\tfrac{1+\xi}{2}\right)h_j f_{j-1/2}^{n-1}(v_j+z_{j-1})f_{j-1/2}^{n-1} + \\
&\tfrac{1}{2}\tfrac{1}{\rho_{Hnf}}\left((1-\omega_2)[(1-\omega_1)\rho_f + \omega_1\tfrac{\rho_{s1}\beta_{s1}}{\beta_f}] + \omega_2\tfrac{\rho_{s1}\beta_{s2}}{\beta_f}\right)\tfrac{\sin\eta^{n-1/2}}{\eta^{n-1/2}}h_j(s_j+s_{j-1}) = (L_1)_{j-1/2}^{n-1}
\end{aligned} \tag{34}$$

$$\begin{aligned}
&\tfrac{1}{\mathrm{Pr}}\left[\frac{k_{Hnf}/k_f}{(1-\omega_2)[(1-\omega_1)+\omega_1(\rho Cp)_1/(\rho Cp)_f]+\omega_2(\rho Cp)_{s2}/(\rho Cp)_f}\right]\left(t_j - t_{j-1}\right) - \\
&\tfrac{\xi}{4}h_j(u_j+u_{j-1}^n)(s_j+s_{j-1}) + (1+\xi+\eta\cot\eta)\tfrac{1}{4}h_j(f_j+f_{j-1})(t_j+t_{j-1}) + \tfrac{\xi}{2}h_j(u_j+u_{j-1})s_{j-1/2}^{n-1} - \\
&\tfrac{\xi}{2}h_j u_{j-1/2}^{n-1}(s_j+s_{j-1}) - \tfrac{\xi}{2}h_j(t_j-t_{j-1})f_{j-1/2}^{n-1} + \tfrac{\xi}{2}h_j t_{j-1/2}^{n-1}(f_j+f_{j-1}) = (L_2)_{j-1/2}^{n-1}
\end{aligned} \tag{35}$$

$$(l_1)_{j-1/2}^{n-1} = -h_j\left(\begin{array}{l}
\frac{\rho_f}{\rho_{Hnf}}\left(\frac{1}{(1-\omega_1)^{2.5}(1-\omega_2)^{2.5}}\right)\frac{\left(v_j - v_{j-1}\right)}{h_j} + \\
\mathrm{We}\; v_{j-1}v'_{j-1/2}(1-\xi+\eta\cot\eta)f_{j-1/2}v_{j-1/2} + (\xi-1)\left(u_{j-1/2}\right)^2 - \frac{\rho_f\sigma_{nf}}{\rho_{nf}\sigma_f}\,\mathrm{M}u_{j-1/2} + \\
\left((1-\omega_2)[(1-\omega_1)\rho_f + \omega_1\frac{\rho_{s1}\beta_{s1}}{\beta_f}] + \omega_2\frac{\rho_{s1}\beta_{s2}}{\beta_f}\right)\frac{\sin\eta^{n-1/2}}{\eta^{n-1/2}}s_{j-1/2}
\end{array}\right)^{n-1} \tag{36}$$

$$(l_2)_{j-1/2}^{n-1} = -h_j\left(\begin{array}{l}
\frac{1}{\mathrm{Pr}}\left[\frac{k_{Hnf}/k_f}{(1-\omega_2)[(1-\omega_1)+\omega_1(\rho Cp)_1/(\rho Cp)_f]+\omega_2(\rho Cp)_{s2}/(\rho Cp)_f}\right]\frac{\left(t_j - t_{j-1}\right)}{h_j} \\
+(1+\eta\cot\eta-\xi)f_{j-1/2}t_{j-1/2} + \xi u_{j-1/2}s_{j-1/2}
\end{array}\right)^{n-1} \tag{37}$$

where $\xi = \frac{\eta^{n-1/2}}{k_n}$.

The boundary condition can be written as:

$$f_0^n = u_0^n = 0,\; t_0^n = 1, u_J^n = s_J^n = 0, \tag{38}$$

Subsequently, the mathematical formula for the previous system (31)–(35) of non-linear algebraic equations will be linearized, by using Newton's known method, and then solved by the block elimination technique. Furthermore, the numerical results are obtained by programming the algorithm of a linear system executed by MATLAB software. When we run the MATLAB program code, it needs to identify some specific computations: the boundary layer thickness y_∞; proper step size Δy; and the step size Δx. y_∞ is almost constant [63]. Furthermore, when $\mathrm{Pr} = 6.2$, in this study, y_∞ suitably lies between 3.5 and 8, to satisfy the boundary layer convergence. Once we obtain the suitable value of y_∞, a sensible option of step size Δy and step size Δx should be determined. So, in the boundary layer flow, the step size $\Delta y = 0.02$ and $\Delta x = 0.005$ are appropriate to acquire accurate approximate numerical results. Moreover, these particular values successfully obtain outcomes which are almost compatible with previous findings, as displayed in Tables 2 and 3.

Table 2. Comparison of the outcomes for Nu at $\mathrm{Pr} = 7$, $\omega_1 = \omega_2 = 0$, $\mathrm{We} = 0$, and $\mathrm{M} = 0$.

η	[64]	[65]	Present
0	0.9581	0.9595	0.9593
$(1/18)\pi$	0.9559	0.9572	0.9568
$(1/9)\pi$	0.9496	0.9506	0.9499
$(1/6)\pi$	0.9389	0.9397	0.9397
$(2/9)\pi$	0.9239	0.9243	0.9242
$(5/18)\pi$	0.9045	0.9045	0.9046
$(1/3)\pi$	0.8858	0.8801	0.8833

Table 2. *Cont.*

η	[64]	[65]	Present
$(7/18)\pi$	0.8518	0.8510	0.8526
$(4/9)\pi$	0.8182	0.8168	0.8178
$(1/2)\pi$	0.7792	0.7792	0.7792

Table 3. Comparison of the outcomes for C_f at Pr $= 7$, $\varpi_1 = \varpi_2 = 0$, We $= 0$, and M $= 0$.

η	[64]	[65]	Present
0	0.0000	0.0000	0.0000
$(1/18)\pi$	0.0876	0.0875	0.0878
$(1/9)\pi$	0.1737	0.1735	0.1737
$(1/6)\pi$	0.2566	0.2563	0.2566
$(2/9)\pi$	0.3350	0.3345	0.3349
$(5/18)\pi$	0.4075	0.4068	0.4076
$(1/3)\pi$	0.4727	0.4715	0.4730
$(7/18)\pi$	0.5293	0.5380	0.5391
$(4/9)\pi$	0.5762	0.5745	0.5760
$(1/2)\pi$	0.6123	0.6103	0.6129

4. Results and Discussion

The current section provides an in-depth analysis of natural convection's physical aspects produced by a magnetized Williamson hybrid nanofluid flowing around a spherical shape by highlighting the impressions of ultrafine particle fraction χ, magnetic parameter M, and Weissenberg number We on physical quantities, as they relate to energy transmission. The pertinent parameters are chosen in the following ranges: $\chi = 0.1,\ 0.15,\ 0.2$; $M = 0.1,\ 0.5,\ 1$; and We $= 0.1,\ 0.4,\ 0.5,\ 0.8$, in addition to fixing the Prandtl number at Pr $= 6.2$ (the Prandtl number for water) throughout the numerical calculations. Table 4 shows the thermophysical properties of H_2O and booster nanosolid as used in this analysis.

Table 4. Thermophysical properties of H_2O and booster nanosolid [25,46,66,67].

Physical Properties	Water	MWCNT	GO	MoS_2
ρ (kg/m^3)	997.1	1600	1800	5060
k (W/mK)	0.613	3000	5000	904.4
cp (J/kgK)	4179	796	717	397.21
σ (Sm^{-1})	5.5×10^{-6}	1.9×10^{-4}	6.30×10^{7}	2.09×10^{4}
$\beta \times 10^{-5}$ (K^{-1})	21	44		2.8424

Figure 3 illustrates the extent to which magnetic parameter intensification affects skin friction of mono and hybrid nanofluids while maintaining the ultrafine particle fraction χ and Weissenberg number We at constant values. Skin friction values decline as magnetic parameter values increase. This decline is due to the restriction in fluid flow produced by a rise in the strength of the magnetic field, which restricts convection and therefore decreases skin friction. Figure 4 describes the influence of the Weissenberg number on skin friction. It is noted that skin friction reduces as the Weissenberg number is elevated, owing to fluid thickening and increased viscous force at high We values. Figure 5 traces the effect of the ultrafine particle volume fraction on the mono/hybrid nanofluid's skin friction, considering that the magnetic parameter and Weissenberg number are fixed values. It has been observed that increasing the ultrafine particle volume fraction tends to reduce skin friction, whether for hybrid or mono-nanofluid. The influence of escalating magnetic parameter values on the Nusselt number is expounded in Figure 6. It indicates that the ascending value of the magnetic parameter reduces the Nusselt number. In reality, increasing the intensity of the magnetic field interrupts the fluid movement, which in turn limits heat transmission. This means a decrease in the Nusselt number. In Figure 7,

a decline in the Nusselt number is associated with an augmentation in the Weissenberg number, which seems to indicate that heat is transported from the spherical surface to the boundary layer, and the temperature is observed to increase with the Weissenberg number. As a result, the spherical surface is efficiently cooled with higher Weissenberg number values. Figure 8 conveys the variations of Nusselt number for various values of the ultrafine particle volume fraction at fixed We = 0.5 and magnetic parameter M = 3. Obviously, increasing the volume fraction of nanoparticles assists in raising the curve of the Nusselt number. More specifically, growth in the volume fraction of ultrafine particles, whether MWCNT or GO, contributes to improving the thermal conductivity of the mono nanofluid MoS_2/water, and as a result, the heat transfer rate increases, and therefore the Nusselt number increases. Moreover, in terms of energy transfer rate, the examined hybrid/mono-nano liquids can be arranged in ascending order regardless of the influencing parameter: MoS_2/H_2O < GO-MoS_2/H_2O < MWCNTs-MoS_2/H_2O. This superiority of composition of the carbon nanotubes and water in terms of the heat transfer rate may be due to the superior thermal conductivity of this nanofluidic hybrid. The behavior of the hybrid nanofluid's temperature under the effect of M is shown in Figure 9. The temperature of the hybrid fluid in the boundary laminar layers increases with the strength of the imposed magnetic field. The main reason behind this dramatic rise in temperature profiles is the Lorentz force generated by the crossing transverse magnetic field, which in turn increases the friction and consequently elevates the temperature of the hybrid nanofluid. The influence of the Weissenberg number We on temperature is seen in Figure 10. It is worth noting that the temperature of the nanofluid rises as its values escalate. This occurs due to the higher resistance caused by the increased viscosity. Figure 11 describes the impression of ultrafine particle volume fraction variation on the hybrid nanofluid's temperature. An elevation in the volume fraction of ultrafine particles produces an increase in heat transmission from the sphere's surface to the host liquid, which aids in increasing the thermal boundary layer thickness. Figure 12 contains graphical results for the critical impact of magnetic parameters on the hybrid nanofluid's velocity. This is known as the Lorentz force phenomenon, something which occurs when the magnetic field crosses a flowing fluid, and where this force restrains the movement of the fluid, slowing it down. In Figure 13, the flow of the nanofluid is found to diminish when the Weissenberg number is raised, implying that the velocity of the nanofluid is inhibited. This restriction in fluid movement is attributed to increased viscosity effects. The variation of velocity curves together with the ultrafine particle volume fraction values escalated are reported in Figure 14. The rise in the volume fraction leads to enhanced energy transfer, which in turn raises the fluid's velocity.

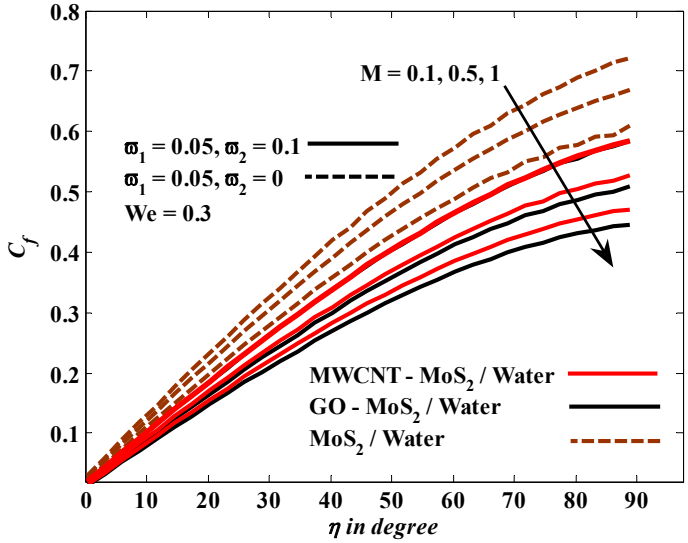

Figure 3. The behavior of hybrid nanofluid's skin friction under the effect of *M*.

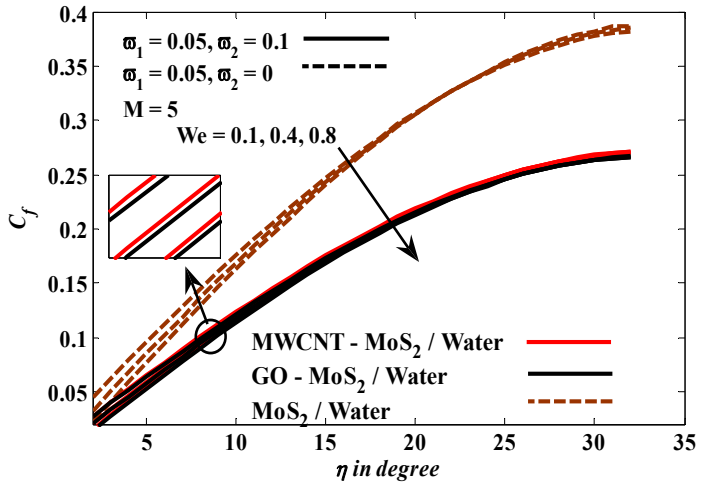

Figure 4. The behavior of mono-hybrid nanofluid's skin friction under the effect of We.

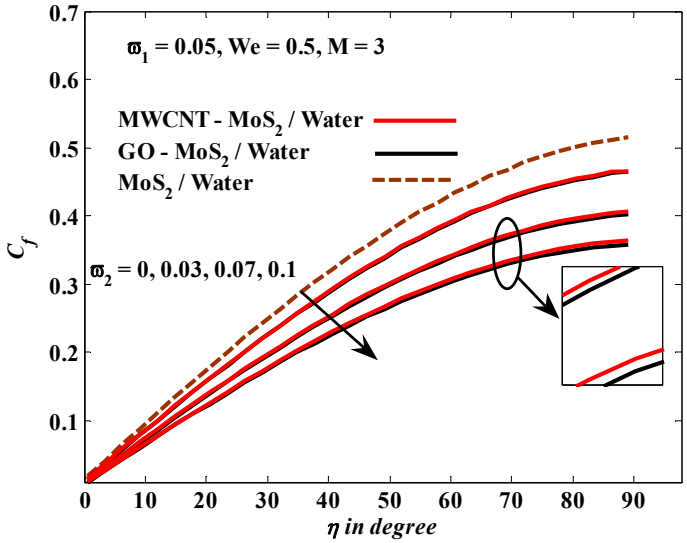

Figure 5. The behavior of hybrid nanofluid's skin friction under the effect of ultrafine particle volume fraction.

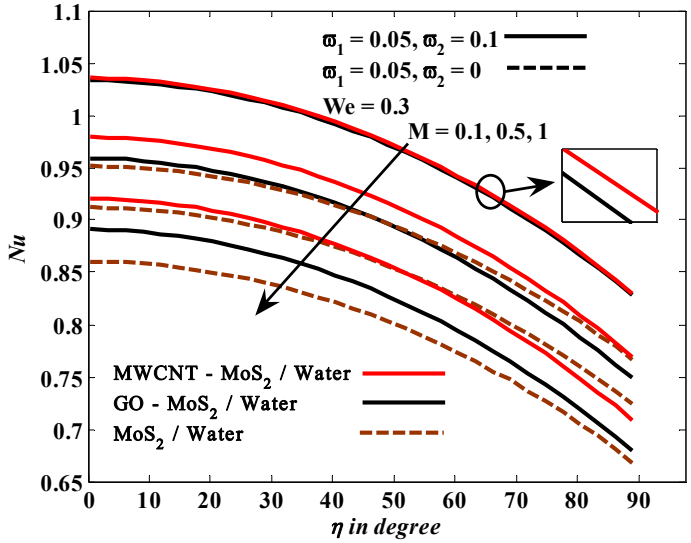

Figure 6. The behavior of hybrid nanofluid's Nusselt number under the effect of *M*.

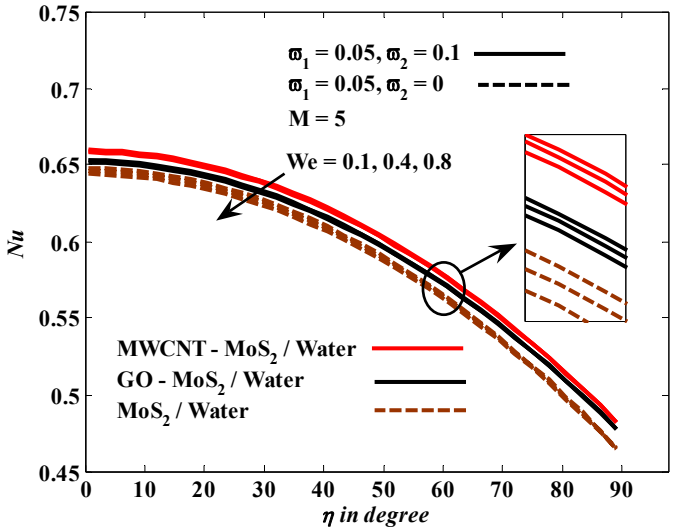

Figure 7. The behavior of hybrid nanofluid's Nusselt number under the effect of We.

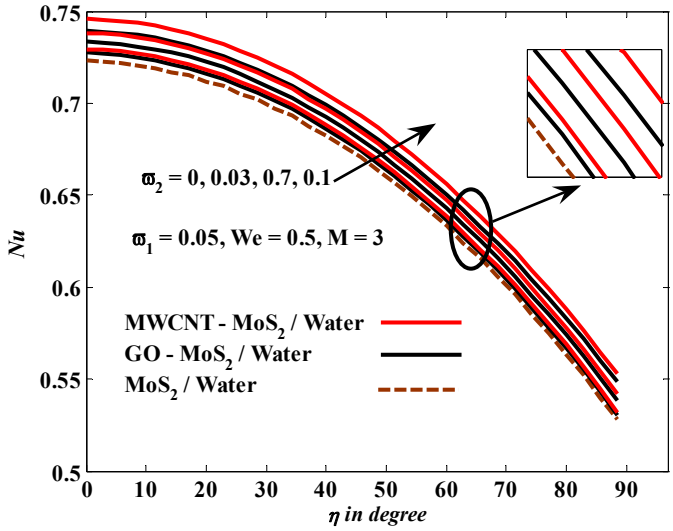

Figure 8. The behavior of hybrid nanofluid's Nusselt number under the effect of ultrafine particle volume fraction.

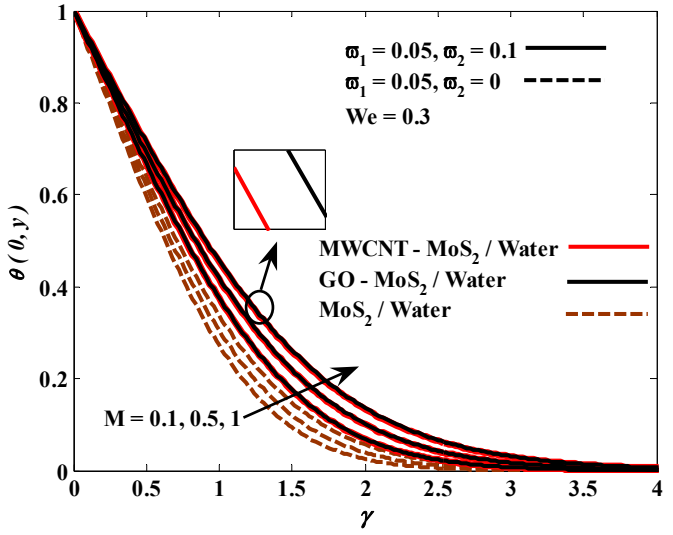

Figure 9. The behavior of hybrid nanofluid's temperature under the effect of M.

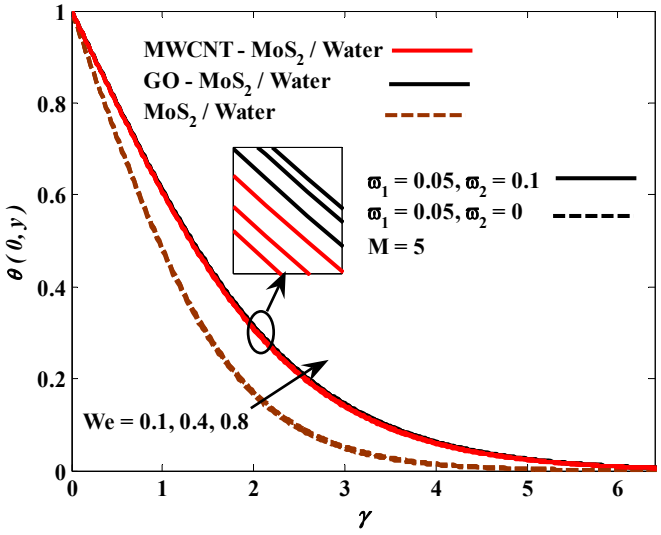

Figure 10. The behavior of hybrid nanofluid's temperature under the effect of We.

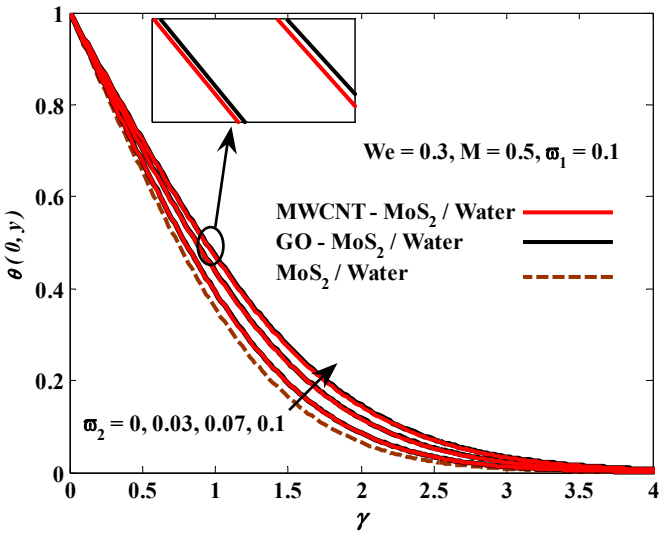

Figure 11. The behavior of hybrid nanofluid's temperature under the effect of ultrafine particle volume fraction.

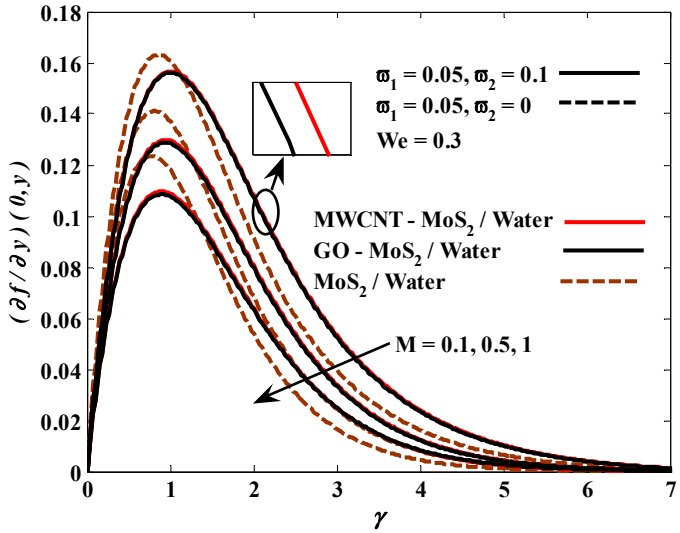

Figure 12. The behavior of hybrid nanofluid's velocity under the effect of M.

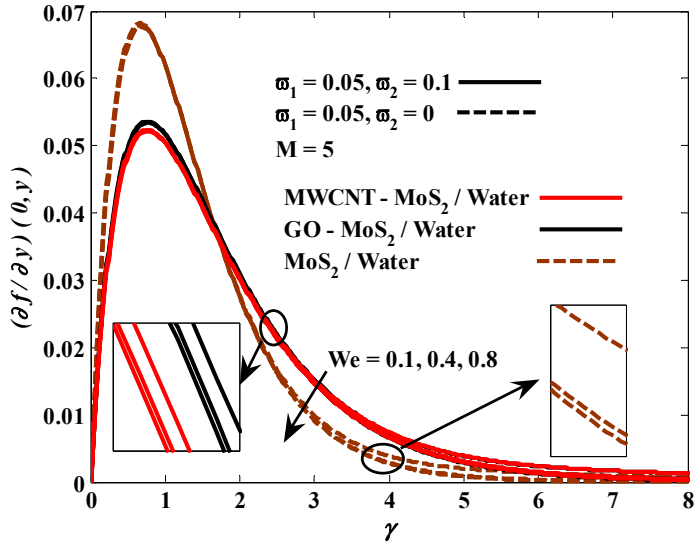

Figure 13. The behavior of hybrid nanofluid's velocity under the effect of We.

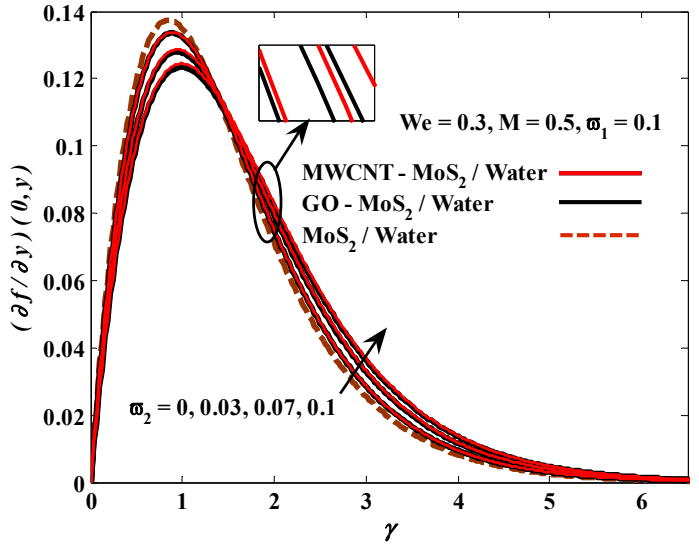

Figure 14. The behavior of hybrid nanofluid's velocity under the effect of ultrafine particle volume fraction.

5. Conclusions

The energy transfer of Williamson fluid flowing around a spherical shape supported by upgraded promoter nanosolid in the case of MHD convection produced by natural means was simulated computationally. It yielded the following meaningful points:

1- The use of hybrid nanosolids stimulates energy transfer through the host fluid;
2- The Weissenberg number has a positive effect on temperature and friction drag, while it negatively affects energy transfer and fluid velocity;
3- Growing the strength of the magnetic field decreases velocity, friction drag, and energy transfer rate but raises temperature;
4- Increasing the volume fraction of catalyzed nanomaterials (whether for MWCNTs or GO) improves energy transfer, raises the fluid temperature, and reduces friction drag;
5- In terms of energy transfer rate, the examined hybrid/mono-nano liquids can be arranged in ascending order regardless of the influencing parameter as:

$$MoS_2/H_2O < GO\text{-}MoS_2/H_2O < MWCNTs\text{-}MoS_2/H_2O.$$

Author Contributions: O.A.S.A.: Writing—original draft, Resources, Investigation; F.A.A.: Conceptualization, Validation, Writing and editing; I.M.S.: Writing—original draft, Resources; M.Z.S.: Methodology, Software, Formal analysis; A.S.H.: Writing—original draft, Investigation; M.A.H.I.: validation, write—review and editing. All authors have read and agreed to the published version of the manuscript.

Funding: This research received no external funding.

Data Availability Statement: Not applicable.

Conflicts of Interest: The authors declare that they have no conflict of interest.

Abbreviations

The symbols and their indications:

a	Radius of spherical shape
B_o	Magnetic field intensity
C_f	Skin friction
C_p	Heat capacity
$r(\eta)$	Radial distance
g	Gravity vector
Gr	Grashof number
k_f	Thermal conductivity
M	Magnetic parameter
Nu	Nusselt number
Pr	Prandtl number
Re	Reynold number
T	Base liquid temperature
T_∞	Surrounding temperature
u	$\eta-$ component of velocity
v	$\gamma-$ component of velocity
v_f	Kinematic viscosity
We	Weissenberg number
α	Thermal diffusivity
β	Thermal expansion
Γ	Fluid relaxation time
σ	Electrical conductivity
θ	Temperature
μ	Dynamic viscosity
ρ	Density
$\overline{\omega}$	Volume fraction of nanosolid
τ_w	Wall shear stress
ψ	Stream transformation
σ	Electrical conductivity
Subscript	
f	Host liquid
Hnf	Hybrid nanoliquid
nf	Nanoliquid
$\overline{\omega}_1$	Volume fraction of MWCNTs or GO
$\overline{\omega}_2$	Volume fraction of MoS_2

References

1. Williamson, R.V. The flow of pseudoplastic materials. *Ind. Eng. Chem.* **1929**, *21*, 1108–1111. [CrossRef]
2. Lyubimov, D.; Perminov, A. Motion of a thin oblique layer of a pseudoplastic fluid. *J. Eng. Phys. Thermophys.* **2002**, *75*, 920–924. [CrossRef]
3. Nadeem, S.; Akram, S. Peristaltic flow of a Williamson fluid in an asymmetric channel. *Commun. Nonlinear Sci. Numer. Simul.* **2010**, *15*, 1705–1716. [CrossRef]
4. Nadeem, S.; Hussain, S. Flow and heat transfer analysis of Williamson nanofluid. *Appl. Nanosci.* **2014**, *4*, 1005–1012. [CrossRef]
5. Hayat, T.; Kiyani, M.; Alsaedi, A.; Khan, M.I.; Ahmad, I. Mixed convective three-dimensional flow of Williamson nanofluid subject to chemical reaction. *Int. J. Heat Mass Transf.* **2018**, *127*, 422–429. [CrossRef]

6. Subbarayudu, K.; Suneetha, S.; Reddy, P.B.A. The assessment of time dependent flow of Williamson fluid with radiative blood flow against a wedge. *Propuls. Power Res.* **2020**, *9*, 87–99. [CrossRef]
7. Waqas, M.; Khan, M.I.; Asghar, Z.; Kadry, S.; Chu, Y.-M.; Khan, W. Interaction of heat generation in nonlinear mixed/forced convective flow of Williamson fluid flow subject to generalized Fourier's and Fick's concept. *J. Mater. Res. Technol.* **2020**, *9*, 11080–11086. [CrossRef]
8. Hayat, T.; Bashir, G.; Waqas, M.; Alsaedi, A. MHD 2D flow of Williamson nanofluid over a nonlinear variable thicked surface with melting heat transfer. *J. Mol. Liq.* **2016**, *223*, 836–844. [CrossRef]
9. Choi, S.U.; Eastman, J.A. *Enhancing Thermal Conductivity of Fluids with Nanoparticles*; Argonne National Lab. (ANL): Argonne, IL, USA, 1995.
10. Eastman, J.A.; Choi, S.; Li, S.; Yu, W.; Thompson, L. Anomalously increased effective thermal conductivities of ethylene glycol-based nanofluids containing copper nanoparticles. *Appl. Phys. Lett.* **2001**, *78*, 718–720. [CrossRef]
11. Chon, C.H.; Kihm, K.D.; Lee, S.P.; Choi, S.U. Empirical correlation finding the role of temperature and particle size for nanofluid (Al 2 O 3) thermal conductivity enhancement. *Appl. Phys. Lett.* **2005**, *87*, 153107. [CrossRef]
12. Xuan, Y.; Li, Q. Heat transfer enhancement of nanofluids. *Int. J. Numer. Methods Heat Fluid Flow* **2000**, *21*, 58–64. [CrossRef]
13. Wang, X.-Q.; Mujumdar, A.S. Heat transfer characteristics of nanofluids: A review. *Int. J. Therm. Sci.* **2007**, *46*, 1–19. [CrossRef]
14. Trisaksri, V.; Wongwises, S. Critical review of heat transfer characteristics of nanofluids. *Ren. Sustain. Energy Rev.* **2007**, *11*, 512–523. [CrossRef]
15. Putra, N.; Roetzel, W.; Das, S. Natural convection of nano-fluids. *Heat Mass Transf.* **2003**, *39*, 775–784. [CrossRef]
16. Tiwari, R.K.; Das, M.K. Heat transfer augmentation in a two-sided lid-driven differentially heated square cavity utilizing nanofluids. *Int. J. Heat Mass Transf.* **2007**, *50*, 2002–2018. [CrossRef]
17. Tham, L.; Nazar, R.; Pop, I. Mixed convection boundary-layer flow about an isothermal solid sphere in a nanofluid. *Phys. Scr.* **2011**, *84*, 025403. [CrossRef]
18. Tham, L.; Nazar, R.; Pop, I. Mixed convection boundary layer flow from a horizontal circular cylinder in a nanofluid. *Int. J. Numer. Method H.* **2012**, *22*, 576–606. [CrossRef]
19. Dinarvand, S.; Hosseini, R.; Pop, I. Axisymmetric mixed convective stagnation-point flow of a nanofluid over a vertical permeable cylinder by Tiwari-Das nanofluid model. *Powder Technol.* **2017**, *311*, 147–156. [CrossRef]
20. Swalmeh, M.Z.; Alkasasbeh, H.T.; Hussanan, A.; Mamat, M. Heat transfer flow of Cu-water and Al2O3-water micropolar nanofluids about a solid sphere in the presence of natural convection using Keller-box method. *Res. Phys.* **2018**, *9*, 717–724. [CrossRef]
21. Swalmeh, M.Z.; Alkasasbeh, H.T.; Hussanan, A.; Mamat, M. Numerical investigation of heat transfer enhancement with Ag-GO water and kerosene oil based micropolar nanofluid over a solid sphere. *J. Adv. Res. Fluid Mech. Therm. Sci.* **2019**, *59*, 269–282.
22. Swalmeh, M.Z.; Alkasasbeh, H.T.; Hussanan, A.; Mamat, M. Influence of micro-rotation and micro-inertia on nanofluid flow over a heated horizontal circular cylinder with free convection. *Theor. Appl. Mech.* **2019**, *46*, 125–145. [CrossRef]
23. Alwawi, F.A.; Alkasasbeh, H.T.; Rashad, A.; Idris, R. MHD natural convection of Sodium Alginate Casson nanofluid over a solid sphere. *Res. Phys.* **2020**, *16*, 102818. [CrossRef]
24. Alwawi, F.A.; Alkasasbeh, H.T.; Rashad, A.M.; Idris, R. A numerical approach for the heat transfer flow of carboxymethyl cellulose-water based Casson nanofluid from a solid sphere generated by mixed convection under the influence of Lorentz force. *Mathematics* **2020**, *8*, 1094. [CrossRef]
25. Alwawi, F.A.; Alkasasbeh, H.T.; Rashad, A.; Idris, R. Heat transfer analysis of ethylene glycol-based Casson nanofluid around a horizontal circular cylinder with MHD effect. *Proc. Inst. Mech. Eng. C J. Mech. Eng. Sci.* **2020**, *234*, 2569–2580. [CrossRef]
26. Alwawi, F.A.; Alkasasbeh, H.T.; Rashad, A.M.; Idris, R. Natural convection flow of Sodium Alginate based Casson nanofluid about a solid sphere in the presence of a magnetic field with constant surface heat flux. In Proceedings of the Journal of Physics: Conference Series, Ningbo, China, 1–3 July 2019; p. 012005.
27. Alwawi, F.; Sulaiman, I.M.; Swalmeh, M.Z.; Yaseen, N. Energy transport boosters of magneto micropolar fluid flowing past a cylinder: A case of laminar combined convection. *Proc. Inst. Mech. Eng. C J. Mech. Eng. Sci.* **2022**, *236*, 10902–10913. [CrossRef]
28. Hamarsheh, A.S.; Alwawi, F.A.; Alkasasbeh, H.T.; Rashad, A.M.; Idris, R. Heat transfer improvement in MHD natural convection flow of graphite oxide/carbon nanotubes-methanol based casson nanofluids past a horizontal circular cylinder. *Processes* **2020**, *8*, 1444. [CrossRef]
29. Alwawi, F.A.; Hamarsheh, A.S.; Alkasasbeh, H.T.; Idris, R. Mixed Convection Flow of Magnetized Casson Nanofluid over a Cylindrical Surface. *Coatings* **2022**, *12*, 296. [CrossRef]
30. Khan, U.; Zaib, A.; Pop, I.; Waini, I.; Ishak, A. MHD flow of a nanofluid due to a nonlinear stretching/shrinking sheet with a convective boundary condition: Tiwari–Das nanofluid model. *Int. J. Numer. Method H* **2022**. *ahead-of-print*. [CrossRef]
31. Swalmeh, M.Z.; Shatat, F.; Alwawi, F.A.; Ibrahim, M.A.H.; Sulaiman, I.M.; Yaseen, N.; Naser, M.F. Effectiveness of Radiation on Magneto-Combined Convective Boundary Layer Flow in Polar Nanofluid around a Spherical Shape. *Fractal Fract.* **2022**, *6*, 383. [CrossRef]
32. Yaseen, N.; Shatat, F.; Alwawi, F.A.; Swalmeh, M.Z.; Kausar, M.S.; Sulaiman, I.M. Using Micropolar Nanofluid under a Magnetic Field to Enhance Natural Convective Heat Transfer around a Spherical Body. *J. Adv. Res. Fluid Mech. Therm. Sci.* **2022**, *96*, 179–193. [CrossRef]

33. Turcu, R.; Darabont, A.; Nan, A.; Aldea, N.; Macovei, D.; Bica, D.; Vekas, L.; Pana, O.; Soran, M.; Koos, A. New polypyrrole-multiwall carbon nanotubes hybrid materials. *J. Optoelectron. Adv. Mater.* **2006**, *8*, 643–647.
34. Suresh, S.; Venkitaraj, K.; Selvakumar, P.; Chandrasekar, M. Synthesis of Al2O3–Cu/water hybrid nanofluids using two step method and its thermo physical properties. *Colloids Surf. A Physicochem. Eng. Asp.* **2011**, *388*, 41–48. [CrossRef]
35. Baghbanzadeh, M.; Rashidi, A.; Rashtchian, D.; Lotfi, R.; Amrollahi, A. Synthesis of spherical silica/multiwall carbon nanotubes hybrid nanostructures and investigation of thermal conductivity of related nanofluids. *Thermochim. Acta* **2012**, *549*, 87–94. [CrossRef]
36. Zhou, W.; Chen, Q.; Sui, X.; Dong, L.; Wang, Z. Enhanced thermal conductivity and dielectric properties of Al/β-SiCw/PVDF composites. *Compos. Part A Appl. Sci. Manuf.* **2015**, *71*, 184–191. [CrossRef]
37. Leong, K.; Ahmad, K.K.; Ong, H.C.; Ghazali, M.; Baharum, A. Synthesis and thermal conductivity characteristic of hybrid nanofluids–a review. *Ren. Sustain. Energy Rev.* **2017**, *75*, 868–878. [CrossRef]
38. Chen, L.F.; Cheng, M.; Yang, D.J.; Yang, L. Enhanced thermal conductivity of nanofluid by synergistic effect of multi-walled carbon nanotubes and Fe2O3 nanoparticles. In *Proceedings of the Applied Mechanics and Materials*; Trans Tech Publications Ltd.: Bäch SZ, Switzerland, 2014; pp. 118–123.
39. Esfe, M.H.; Saedodin, S.; Biglari, M.; Rostamian, H. Experimental investigation of thermal conductivity of CNTs-Al2O3/water: A statistical approach. *Int. Commun. Heat Mass Transf.* **2015**, *69*, 29–33. [CrossRef]
40. Yarmand, H.; Gharehkhani, S.; Shirazi, S.F.S.; Goodarzi, M.; Amiri, A.; Sarsam, W.S.; Alehashem, M.S.; Dahari, M.; Kazi, S. Study of synthesis, stability and thermo-physical properties of graphene nanoplatelet/platinum hybrid nanofluid. *Int. Commun. Heat Mass Transf.* **2016**, *77*, 15–21. [CrossRef]
41. Mohamed, A.L.; El-Naggar, M.E.; Hassabo, A.G. Preparation of hybrid nanoparticles to enhance the electrical conductivity and performance properties of cotton fabrics. *J. Mater. Res. Technol.* **2021**, *12*, 542–554. [CrossRef]
42. Devi, S.A.; Devi, S.S.U. Numerical investigation of hydromagnetic hybrid Cu–Al2O3/water nanofluid flow over a permeable stretching sheet with suction. *Int. J. Nonlinear Sci. Numer. Simul.* **2016**, *17*, 249–257. [CrossRef]
43. Hayat, T.; Nadeem, S. Heat transfer enhancement with Ag–CuO/water hybrid nanofluid. *Res. Phys.* **2017**, *7*, 2317–2324. [CrossRef]
44. Subhani, M.; Nadeem, S. Numerical analysis of micropolar hybrid nanofluid. *Appl. Nanosci.* **2019**, *9*, 447–459. [CrossRef]
45. Khashi'ie, N.S.; Arifin, N.M.; Pop, I.; Wahid, N.S. Flow and heat transfer of hybrid nanofluid over a permeable shrinking cylinder with Joule heating: A comparative analysis. *Alex. Eng. J.* **2020**, *59*, 1787–1798. [CrossRef]
46. Alwawi, F.A.; Swalmeh, M.Z.; Qazaq, A.S.; Idris, R. Heat Transmission Reinforcers Induced by MHD Hybrid Nanoparticles for Water/Water-EG Flowing over a Cylinder. *Coatings* **2021**, *11*, 623. [CrossRef]
47. Jamshed, W.; Mishra, S.; Pattnaik, P.; Nisar, K.S.; Devi, S.S.U.; Prakash, M.; Shahzad, F.; Hussain, M.; Vijayakumar, V. Features of entropy optimization on viscous second grade nanofluid streamed with thermal radiation: A Tiwari and Das model. *Case Stud. Therm. Eng.* **2021**, *27*, 101291. [CrossRef]
48. Jamshed, W.; Prakash, M.; Hussain, S.M.; Eid, M.R.; Nisar, K.S.; Muhammad, T. Entropy amplified solitary phase relative probe on engine oil based hybrid nanofluid. *Chin. J. Phys.* **2022**, *77*, 1654–1681. [CrossRef]
49. Jamshed, W.; Nisar, K.S.; Ibrahim, R.W.; Mukhtar, T.; Vijayakumar, V.; Ahmad, F. Computational frame work of Cattaneo-Christov heat flux effects on Engine Oil based Williamson hybrid nanofluids: A thermal case study. *Case Stud. Therm. Eng.* **2021**, *26*, 101179. [CrossRef]
50. Alwawi, F.A.; Al Faqih, F.M.; Swalmeh, M.Z.; Ibrahim, M.A.H. Combined Convective Energy Transmission Performance of Williamson Hybrid Nanofluid over a Cylindrical Shape with Magnetic and Radiation Impressions. *Mathematics* **2022**, *10*, 3191. [CrossRef]
51. Ali, H.M. *Hybrid Nanofluids for Convection Heat Transfer*; Academic Press: Cambridge, MA, USA, 2020.
52. Esfe, M.H.; Bahiraei, M.; Mir, A. Application of conventional and hybrid nanofluids in different machining processes: A critical review. *Adv. Colloid Interface Sci.* **2020**, *282*, 102199. [CrossRef]
53. Avinash Kumar, R.; Kavitha, M.; Manoj Kumar, P.; Arvindh Seshadri, S. Numerical study of graphene-platinum hybrid nanofluid in microchannel for electronics cooling. *Proc. Inst. Mech. Eng. C J. Mech. Eng. Sci.* **2021**, *235*, 5845–5857. [CrossRef]
54. Roos, H.-G.; Stynes, M.; Tobiska, L. *Robust Numerical Methods for Singularly Perturbed Differential Equations: Convection-Diffusion-Reaction and Flow Problems*; Springer Science & Business Media: Berlin, Germany, 2008; Volume 24.
55. Stynes, M.; Stynes, D. *Convection-Diffusion Problems*; American Mathematical Soc.: Providence, RI, USA, 2018; Volume 196.
56. John, V.; Knobloch, P.; Novo, J. Finite elements for scalar convection-dominated equations and incompressible flow problems: A never ending story? *Comput. Vis. Sci.* **2018**, *19*, 47–63. [CrossRef]
57. AbdulRidha, M.W.; Kashkool, H.A. Space-time petrov-discontinuous galerkin finite element method for solving linear convection-diffusion problems. In Proceedings of the Journal of Physics: Conference Series, Varna, Bulgaria, 21–24 June 2022; p. 012007.
58. Siryk, S. Analysis of lumped approximations in the finite-element method for convection–diffusion problems. *Cybern. Syst. Anal.* **2013**, *49*, 774–784. [CrossRef]
59. Swalmeh, M.Z. Numerical Solutions of Hybrid Nanofluids Flow Via Free Convection Over a Solid Sphere. *J. Adv. Res. Fluid Mech. Therm. Sci.* **2021**, *83*, 34–45. [CrossRef]
60. Yahya, A.U.; Salamat, N.; Huang, W.-H.; Siddique, I.; Abdal, S.; Hussain, S. Thermal charactristics for the flow of Williamson hybrid nanofluid (MoS2+ ZnO) based with engine oil over a streched sheet. *Case Stud. Therm. Eng.* **2021**, *26*, 101196. [CrossRef]

61. Molla, M.M.; Hossain, M.A.; Paul, M.C. Natural convection flow from an isothermal horizontal circular cylinder in presence of heat generation. *Int. J. Eng. Sci.* **2006**, *44*, 949–958. [CrossRef]
62. Bergman, T.L.; Bergman, T.L.; Incropera, F.P.; Dewitt, D.P.; Lavine, A.S. *Fundamentals of Heat and Mass Transfer*; John Wiley & Sons: New York, NY, USA, 2011.
63. Cebeci, T.; Bradshaw, P. *Physical and Computational Aspects of Convective Heat Transfer*; Springer Science & Business Media: Berlin, Germany, 2012.
64. Huang, M.; Chen, G. Laminar free convection from a sphere with blowing and suction. *J. Heat Transf.* **1987**, *109*, 529–532. [CrossRef]
65. Nazar, R.; Amin, N. Free convection boundary layer on an isothermal sphere in a micropolar fluid. *Int. Commun. Heat Mass Transf.* **2002**, *29*, 377–386. [CrossRef]
66. Khan, I.; Gul, A.; Shafie, S. Effects of magnetic field on molybdenum disulfide nanofluids in mixed convection flow inside a channel filled with a saturated porous medium. *J. Porous Media* **2017**, *20*, 435–448. [CrossRef]
67. Alsagri, A.S.; Nasir, S.; Gul, T.; Islam, S.; Nisar, K.; Shah, Z.; Khan, I. MHD thin film flow and thermal analysis of blood with CNTs nanofluid. *Coatings* **2019**, *9*, 175. [CrossRef]